

OPEN

# Volcanic history in the Smythii basin based on SELENE radar observation

Ken Ishiyama<sup>1</sup> & Atsushi Kumamoto<sup>2</sup>

Elucidation of the subsurface structure in the Smythii basin on the moon is important for understanding lunar volcanic history. Two lava units (Units 1 and 2) cover this basin. The spatial subsurface structure below Unit 2 is unknown. We used SELENE/Lunar Radar Sounder data to identify four subsurface boundaries at 130, 190, 300, and 420 m depths. The radar is reflected at the paleo-regolith layer sandwiched among lava flows, which is supported by a simple radar reflection/transmission model. The spatial distribution of subsurface boundaries demonstrates the deposition of Unit 2 on the subsidence in Unit 1. A simple loading model explained the maximum depth of subsidence (~500 m) and indicated that lithospheric thickness in the Smythii basin was ~24 km at 3.95 Gya. The estimated growth rate of the lithosphere was ~60 km/Ga during 3.95 to 3.07 Gya. After the formation of the Smythii basin at ~4.11 Gya, Unit 1 and Unit 2 deposited with eruption rates of  $\sim 8.4 \times 10^{-4} \text{ km}^3/\text{yr}$  by 3.95 Gya and  $\sim 7.5 \times 10^{-6} \text{ km}^3/\text{yr}$  by 3.07 Gya respectively. The timing of decline in volcanic activity in the Smythii basin differs from that for the lunar nearside maria, indicating the diversity of volcanism in various lunar areas.

Lunar volcanic history is crucial for understanding lunar thermal evolution<sup>1–4</sup>. After the formation of the moon ~4.5 Gya (i.e. gigayears ago), melt in the lunar magma ocean remained in the lunar mantle and affected the duration of lunar volcanic activity according to the lunar thermal evolution model<sup>5,6</sup>. During the late heavy bombardment period (~4.0–3.8 Gya)<sup>7,8</sup>, many basins formed on the lunar surface, and magma continued to erupt over a long time on the near side (especially in the Procellarum KREEP Terrane area) rather than the far side<sup>3</sup>.

In this study, we focused on the Smythii basin (1°S, 87°E), located between the lunar near and far sides (Fig. 1a). This circular basin<sup>9,10</sup> formed during the Pre-Nectarian era (before 3.92 Gya)<sup>3</sup> and has five ring structures, which are ~130, 185, 270, 370, and 565 km in radius based on photogeologic mapping<sup>11</sup>. After basin formation, lava partially erupted and was deposited inside the basin, forming two mare units: Units 1 and 2 (Fig. 1a)<sup>12,13</sup>. The geological map of Fig. 1a has previously been published in the United States Geological Survey [<https://pubs.er.usgs.gov/publication/i948>].

Based on Apollo 15/X-ray data, Unit 1 is composed of early volcanic material, which is relatively older than that of Unit 2<sup>12</sup>. Unit 2, the young mare unit of the Smythii basin<sup>3</sup>, is located in the northeast part of the basin (Fig. 1a) and is composed of lava of uniform mineral composition (comprising FeO and TiO<sub>2</sub>)<sup>14</sup>. A ridge (hereafter “Ridge A”) following an east–west direction was formed on Unit 2. In general, lunar ridges are formed by a thermal decrease in lunar radius<sup>15</sup> and by lava-flow loading<sup>1,2</sup>. Based on the crater chronology, the age of Unit 2 is 3.14 Ga (i.e. giga-annum or billion years)<sup>3</sup>, but the formation ages of Unit 1 and the Smythii basin have not yet been investigated clearly.

Based on the empirical relationship between the basin’s diameter and depth, the depth of the mare’s bottom (i.e. mare thickness) was estimated to be 1.28 km on average<sup>16</sup>. In addition, the ejecta composition of several craters on Unit 2 suggested that the mare thickness became shallower along the radial distance from the mare centre<sup>17</sup>.

Lunar subsurface structures have been investigated via seismic surveys and radar exploration<sup>18,19</sup>. The SELENE radar exploration detected one subsurface boundary at a depth of ~250 m in Unit 2<sup>18</sup>, and several subsurface boundaries below Unit 2 have also been reported<sup>19</sup>. However, the spatial distribution of these subsurface

<sup>1</sup>National Institute of Technology, Tsuruoka College, 104 Sawada, Inooka, Tsuruoka, Yamagata, 997-8511, Japan.

<sup>2</sup>Department of Geophysics, Graduate School of Science, Tohoku University, 6-3 Aramaki Aoba, Aoba-ku, Sendai, Miyagi, 980-8578, Japan. Correspondence and requests for materials should be addressed to K.I. (email: [ishiyama.ken@tsuruoka-nct.ac.jp](mailto:ishiyama.ken@tsuruoka-nct.ac.jp))

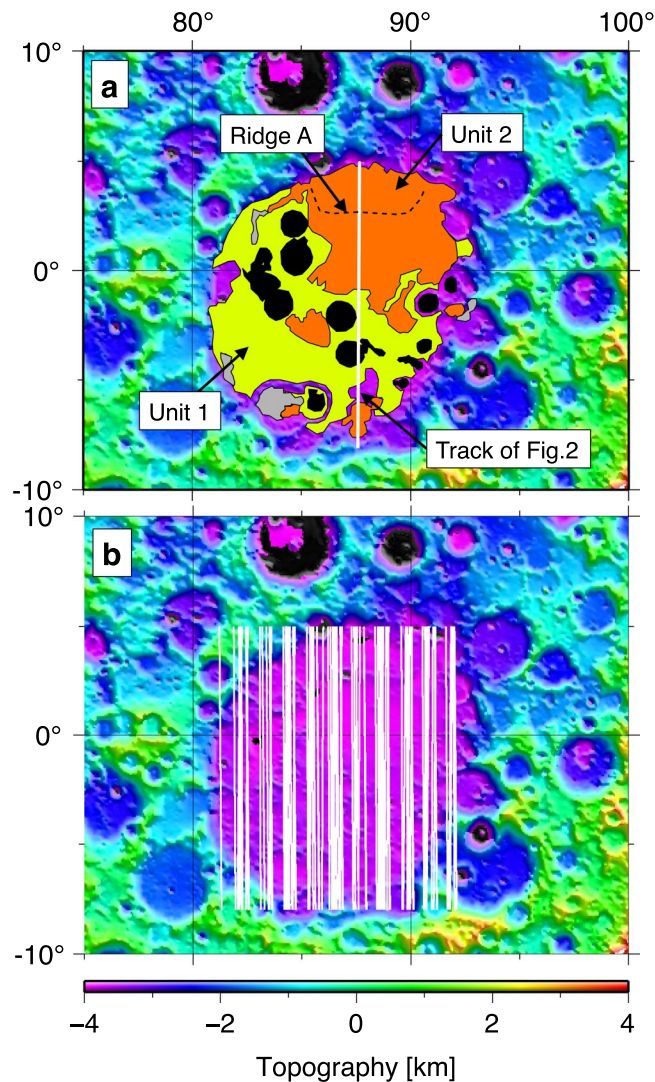
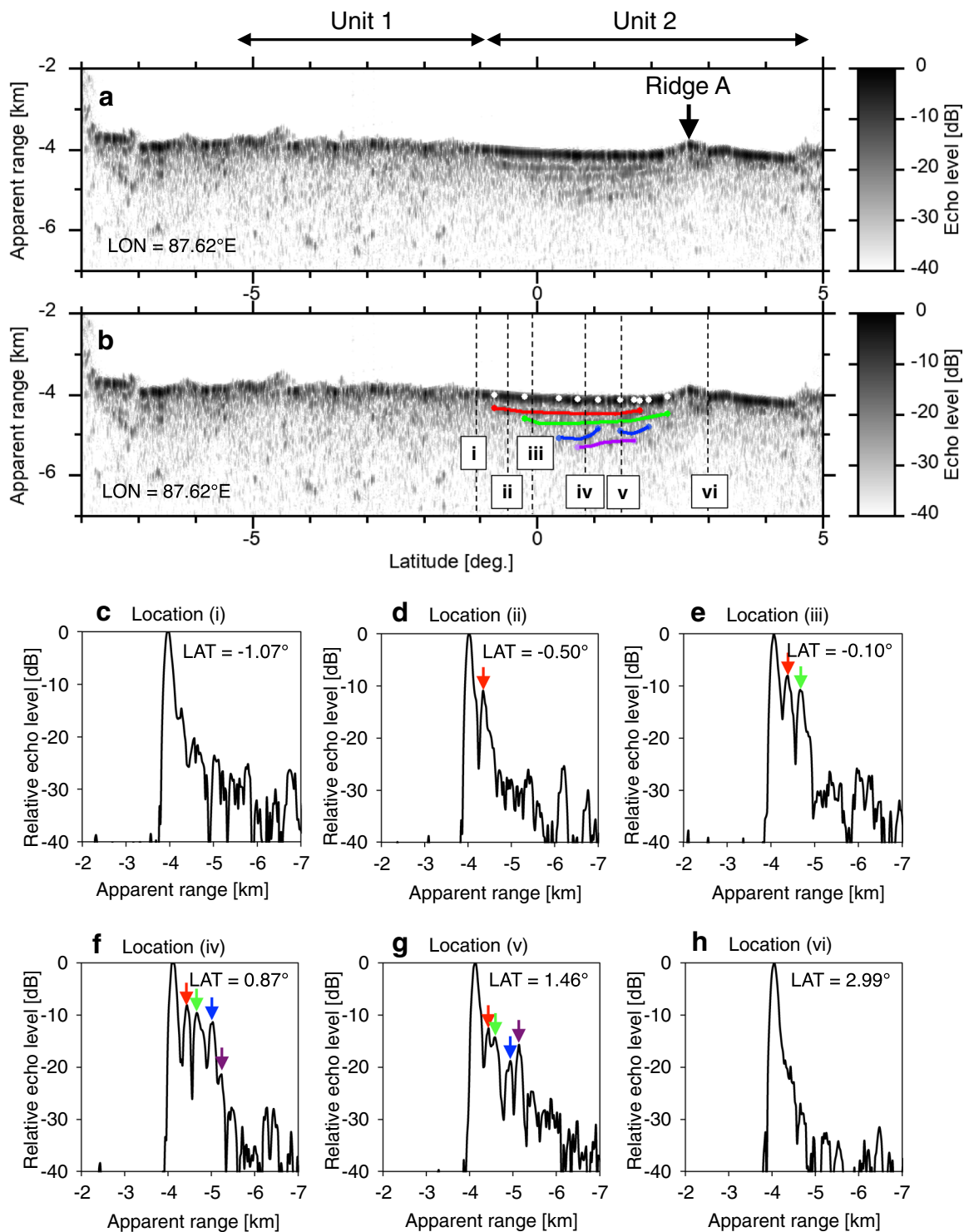


**Figure 1.** Topographical map of the Smythii basin. The background image shows lunar topography, which is created on the basis of SELENE/LALT data<sup>35</sup>. **(a)** Geological map<sup>13</sup> based on the topographical map. The yellow area is Unit 1, the orange area is Unit 2, the grey area is dark mantle deposit, and the black area is where the distinction of units is difficult. The black dotted curve indicates the mare ridge (Ridge A in this study). The white line indicates the SELENE/LRS track used in Fig. 2. **(b)** Spatial distribution of LRS track data used in this study (white lines).

structures has not been investigated. The purpose of this study, therefore, is to identify subsurface boundaries in Unit 2 based on SELENE/Lunar Radar Sounder (LRS) data and to investigate the formation ages of the Smythii basin, Unit 1, and Unit 2. Based on these analyses, we provide suggestions regarding the volcanic history of the Smythii basin. The LRS data covered the area of 8.00°S–5.00°N and 81.00°E–92.00°E (Fig. 1b), which included 90 tracks.

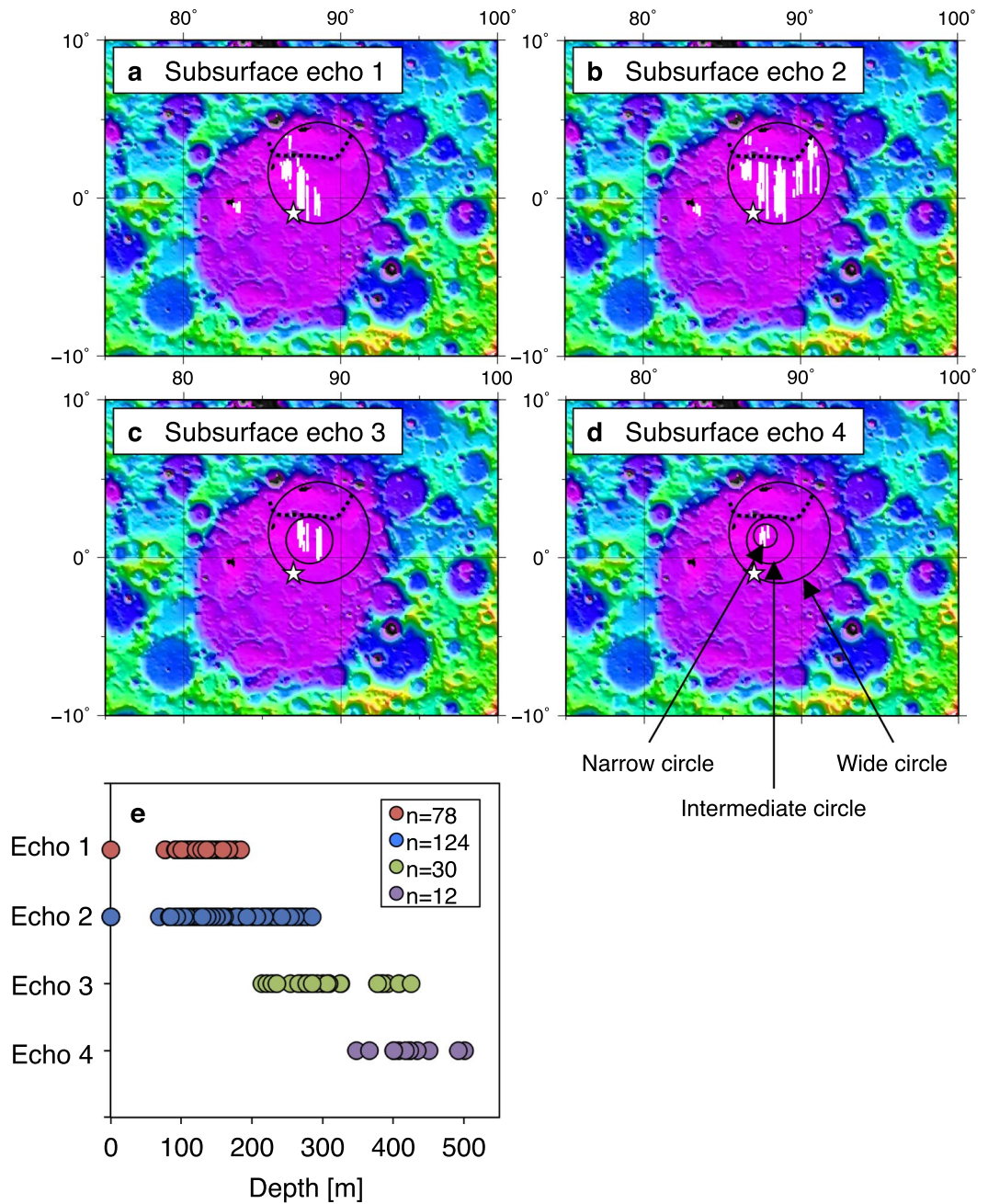
## Results

Fig. 2a,b show the radargram obtained by the LRS data. Other radargrams and these tracks are also shown in Figs S1–S3. We identified four subsurface boundaries in Unit 2, namely subsurface boundaries 1–4. Fig. 2c–h show the echo intensity as a function of depth (i.e. A-scope plot) at locations i–vi, indicated in Fig. 2b. We could not confirm the subsurface echo at locations i and vi (Fig. 2c,h) but identified the clear peaks of subsurface echo in locations ii–v (Fig. 2d–g). Fig. 3a–d show the spatial distributions of the identified subsurface boundaries. The average depths of these subsurface boundaries are  $130 \pm 20$ ,  $190 \pm 60$ ,  $300 \pm 60$ , and  $420 \pm 50$  m, respectively. Fig. 3e shows the range of the measured depth of each subsurface boundary. The deepest subsurface echo was  $\sim 500$  m, located at 0.87°N, 87.41°E (i.e. within the narrowest circle in Fig. 3d). The shallow subsurface boundaries 1 and 2 are widely distributed in Unit 2 (Fig. 3a,b). These subsurface areas have a wide diameter of  $\sim 195$  km, surface area of  $\sim 3.0 \times 10^4$  km<sup>2</sup>, and centre at 1.60°N, 88.60°E (Table S1). The deep subsurface boundaries 3 and 4 are constrained within narrower areas inside the wide circles (Fig. 3c,d). The area of subsurface boundary 3 has an intermediate diameter of 90 km, surface area of  $6.4 \times 10^3$  km<sup>2</sup>, and centre at 1.10°N, 88.00°E. The area



**Figure 2.** Typical radargram obtained from below Unit 2. This figure is created on the basis of SELENE/LRS data. (a) Radargram along 87.62°E (i.e. the white line in Fig. 1a). The colour bar shows the echo level, the horizontal arrows show the range of units, and the down arrow shows the location of Ridge A. (b) Radargram with traced subsurface echoes. The red, green, blue, and purple curves show subsurface boundaries 1–4, respectively. The white points on the surface echo indicate the location of the edges of four subsurface echoes, at which the depths of subsurface echo were measured in this study. The vertical dashed lines indicate locations (i–vi). (c–h) A-scope data at locations (i) (1.07°S), (ii) (0.50°S), (iii) (0.10°S), (iv) (0.87°N), (v) (1.46°N), and (vi) (2.99°N), respectively. The red, green, blue, and purple arrows show the echo peaks of subsurface boundaries 1–4.





**Figure 3.** Spatial distribution of subsurface boundaries 1–4 ((a–d) respectively). The background image shows lunar topography, which is created on the basis of SELENE/LALT data<sup>35</sup>. The white lines show the locations of subsurface boundaries, the white star indicates the geological centre of the Smythii basin (1°S, 87°E), and the black dotted curve shows the location of Ridge A. The black circles (wide, intermediate, and narrow circles) show the areas of each subsurface echo. (e) Measured depth-distribution of subsurface echoes 1–4; “n” is the number of points at which surface and subsurface echoes was observed on a radargram.

of subsurface boundary 4 has a narrow diameter of 45 km, surface area of  $1.6 \times 10^3 \text{ km}^2$ , and centre at 1.40°N, 87.70°E. In addition, most subsurface boundaries were identified on the southern side of Ridge A. The volume of lava below Unit 2 was at least  $(6.6 \pm 2.7) \times 10^3 \text{ km}^3$ , based on the simple multiplication of each layer’s thickness and each subsurface circle area.

Fig. 4a–e show the cumulative crater frequencies for the Smythii basin, Unit 1, and Unit 2. The investigated number of craters (Num) and surface areas (S) are respectively Num = 58 and  $S = 1.1 \times 10^5 \text{ km}^2$  for Smythii basin, Num = 117 and  $S = 6.4 \times 10^3 \text{ km}^2$  for Unit 1, and Num = 314 and  $S = 1.9 \times 10^4 \text{ km}^2$  for Unit 2. Based on the crater chronology (see Method), the model age of the Smythii basin is  $4.11(+0.03/-0.04)$  Ga. The model age of Unit 1 is  $3.95(+0.02/-0.02)$  Ga. An old buried surface aged  $4.02(+0.04/-0.05)$  Ga exists under Unit 1. The model age of Unit 2 is  $3.07(+0.11/-0.16)$  Ga, and an old buried surface aged  $3.89(+0.06/-0.10)$  Ga exists beneath it. Therefore, after the formation of the Smythii basin at  $\sim 4.11$  Gya, Unit 1 deposited by  $\sim 3.95$  Gya, and Unit 2 deposited by  $\sim 3.07$  Gya.

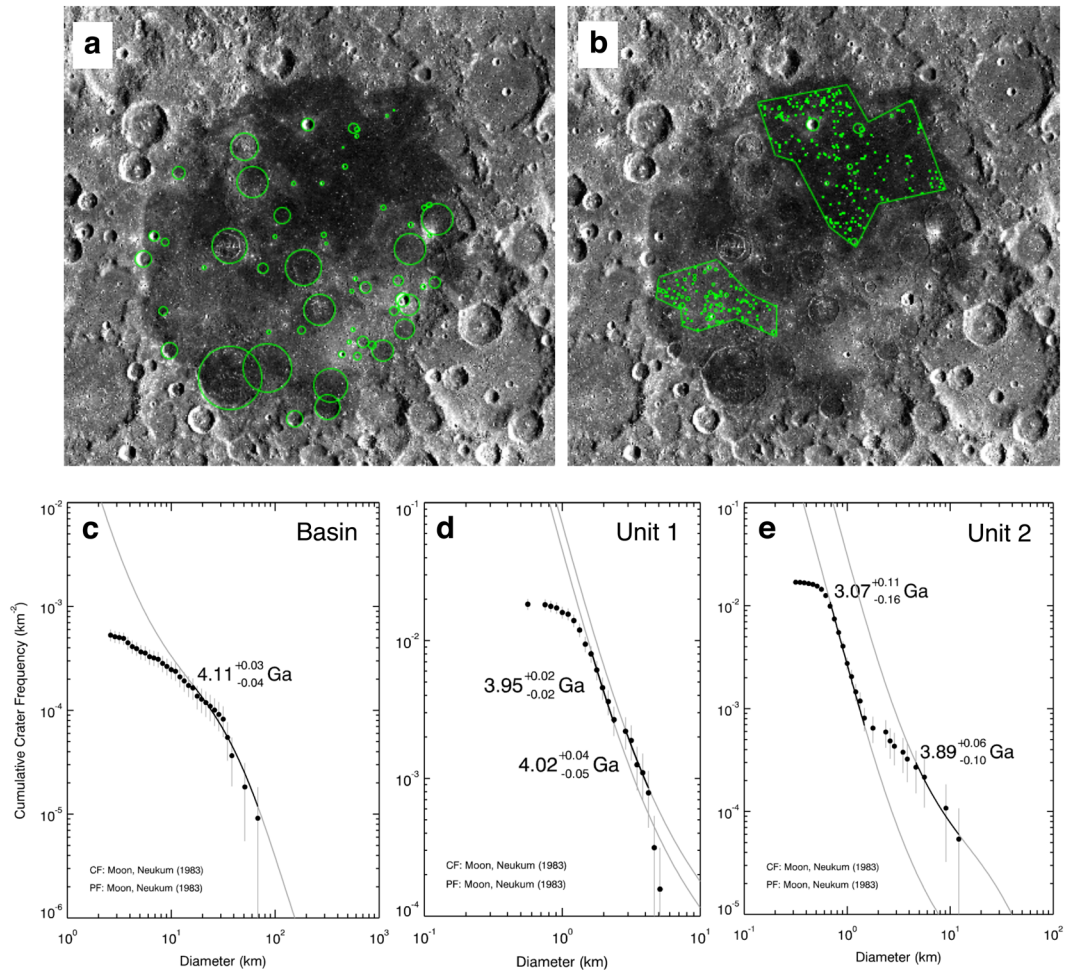


**Figure 4.** Measurement results of crater size-frequency distribution (CSFD) in Mare Smythii. **(a)** The analysed area of Smythii Basin. **(b)** The analysed areas of Units 1 and 2. The background image shows the ortho map, which is created on the basis of the SELENE/TC Ortho data<sup>28</sup>. The green circle shows the location of impact crater. **(c)** The CSFD of Smythii Basin. **(d)** The CSFD of Unit 1. **(e)** The CSFD of Unit 2. The grey curves are of the crater production function polynomial (i.e. PF)<sup>29</sup>. The black curves on the measured CSFD were fitted using the PF, and the suitable model ages were calculated using the cratering chronology function (i.e. CF)<sup>29</sup>.

## Discussion

We first discuss the depths of the subsurface boundaries and the cause of radar reflection. Ono *et al.*<sup>18</sup> found one subsurface boundary below Unit 2 ( $\sim 1.0^\circ\text{N}$ ,  $\sim 87.4^\circ\text{E}$ ), which corresponds to the subsurface boundary 2 in this study. The subsurface boundaries detected in this study are a few hundred metres deep and shallower than the total lava thickness in the Smythii basin (1.28 km)<sup>16</sup>; the LRS detected echoes not from the basin's bottom but from a boundary between the lava layers. In addition, the ejecta composition around the small craters on Unit 2 (Fig. 5 and Table S2) shows an intermediate composition between Units 1 and 2, which indicates that Unit 2 deposited on Unit 1. Craters 4 and 5 locate around the centre of Unit 2, and these ejecta compositions are similar to the composition of Unit 2. This indicates that these craters do not excavate down to the depth of Unit 1; the boundary between Units 1 and 2 is deeper than  $\sim 420$  m at the centre of Unit 2 according to the crater excavation depth ( $d_{\text{exc}} = 0.1 \times 0.84 \times \text{Diameter}$ )<sup>20</sup> (Table S2), which is consistent with the depth of the deepest subsurface echo ( $\sim 500$  m).

Besides, we can expect that the boundary depth between Units 1 and 2 is relatively shallow on the north of Ridge A. For example, Craters 7 and 8 are located at the north of Ridge A, and the composition of Crater 7 is similar to that of Unit 1, while the composition of Crater 8 is similar to that of Unit 2. The excavation depths of these craters, namely  $\sim 210$  m to  $\sim 320$  m for Craters 7 and 8 (Table S2), can restrict the boundary depth between Units 1 and 2 around these craters. This is roughly consistent with the observation result that the shallow subsurface boundaries 1 and 2 slightly exist on the north of Ridge A but the deep subsurface boundaries 3 and 4 do not. We could not extensively determine the thickness of Unit 2 on the north of Ridge A. The reason for a small amount of shallow subsurface boundaries 1 and 2 on the north of Ridge A may be due to the non-uniform thickness of Unit 2 on the area.

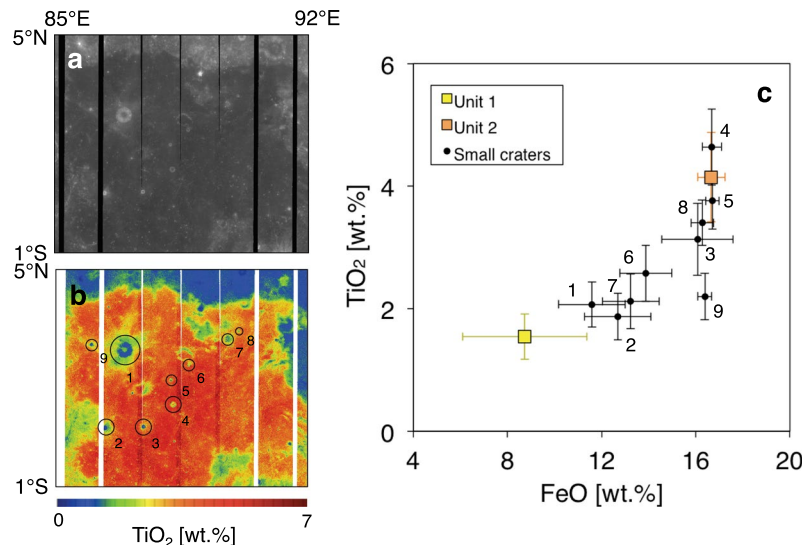


**Figure 5.** Mineral composition around small impact craters on Unit 2. This figure is created on the basis of the SELENE/Multiband Imager (MI) data. (a) 750 nm spectral data based on the MI data. (b) TiO<sub>2</sub> map based on the MI data. This map data was produced on the basis of an algorithm developed in a previous study<sup>22</sup>. The black circles show the locations of measured small craters in this study, and these are numbered in (b,c). (c) Comparison of mineral composition (TiO<sub>2</sub> and FeO) among Unit 1 (yellow square), Unit 2 (orange square), and the small craters in Unit 2 (black point). Unit 1 is that TiO<sub>2</sub> = 1.54 wt.% and FeO = 8.73 wt.%, and Unit 2 is that TiO<sub>2</sub> = 4.15 wt.% and FeO = 16.66 wt.%.

In general, the radar reflection is caused by the permittivity contrast, which is derived from the existence of the regolith layer or the mineral composition contrast (TiO<sub>2</sub> and FeO). In this study, we support the existence of the buried paleo-regolith layer under Unit 2 by using a simple radar reflection/transmission model (Method and Fig. S4). This model uses the following parameters: the contents of TiO<sub>2</sub> and FeO in Units 1 and 2, porosity of Units 1 and 2 ( $\phi$ ), and time delay (i.e. round-trip time) between the surface and subsurface echo ( $\Delta t$ ). The surface mineral compositions are TiO<sub>2</sub> = 1.54 wt.% and FeO = 8.73 wt.% in Unit 1, and TiO<sub>2</sub> = 4.15 wt.% and FeO = 16.66 wt.% in Unit 2 as per the analysis of SELENE/Multiband Imager data<sup>21,22</sup>. Based on these compositions, the estimated bulk permittivity values of Units 1 and 2 are 6.61 and 7.73, respectively. Assuming that  $\phi = 7\%$  based on the Apollo sample<sup>23</sup> and  $\Delta t = 3.33 \times 10^{-6}$  s based on the depth of the deepest subsurface echo (~500 m), the estimated level of the deepest subsurface echo was about  $-35$  dB with respect to the level of surface echo. As shown in Fig. 2, the LRS mainly detected the strong subsurface echoes of  $-20$  dB or more; the mineral composition contrast between Units 1 and 2 cannot explain the observed radar reflection. If a regolith layer exists under Unit 2, the estimated level is about  $-17$  dB, which is close to the level of the deepest subsurface echo (Fig. 2).

The existence of the buried paleo-regolith layer suggests that the lava of Unit 2 was discretely erupted and deposited. Since there are four subsurface boundaries under Unit 2, the lavas erupted at least five separate times. If the lunar lava deposited quickly, the average pause interval between lava eruptions for Unit 2 is  $\sim 0.18$  Ga, which was simply calculated by dividing the formation period of Unit 2 (3.95 to 3.07 Ga) by 5. Thus, this pause interval can contribute to the development of the paleo-regolith layer. After the formation of the Smythii basin at  $\sim 4.11$  Gya, the lava of Unit 1 finished depositing in a short time (by  $\sim 3.95$  Gya); this rapid deposition may explain why the LRS cannot identify the subsurface echoes under Unit 1.

Next, we focused on the spatial distribution of the subsurface boundaries in Unit 2 (Fig. 3). Mare Smythii has semi-major and -minor axes ( $\sim 420$  and  $\sim 330$  km, respectively), and a surface area of  $1.1 \times 10^5$  km<sup>2</sup> (Table S1). The shallow boundaries 1 and 2 lie within the wide circle. The spatial distribution of subsurface boundary 1 is relatively narrower than that of subsurface boundary 2, which indicates that Unit 2 is composed of at least two different subunits. The subsurface boundaries 3 and 4 narrowly distribute within the wide circle. The deepest location of the subsurface boundary was  $0.87^\circ$ N,  $87.41^\circ$ E (i.e. within the smallest circle), which differs from the geological centre of Mare Smythii ( $1.00^\circ$ S,  $87.00^\circ$ E) (see the star in Fig. 3). The spatial structure based on the subsurface circles in Fig. 3 suggests that Unit 2 deposited on a ground subsidence on Unit 1, because the all-subsurface layers are deposited in parallel and the edges of the strata fade with depth, giving the appearance of bowls. We inferred that this subsidence was produced by the loading deflection of Unit 1.

Using a simple loading model<sup>1</sup> (see Method), for example, suppose that Unit 1, with a radius of  $\sim 100$  km (i.e. load), deposited on the lithosphere of thickness ( $T_{\text{litho}} = \sim 24$  km) when Unit 1 formed ( $\sim 3.95$  Gya). Then, we can explain the observed subsidence depth ( $\sim 500$  m). This lithospheric thickness is consistent with the result of Solomon and Head<sup>2</sup>; the lithospheric thickness grows with time. The growth rate of the lithosphere in the Smythii basin is higher than  $\sim 60$  km/Ga during 3.95 to 3.0 Gya, based on the results of this study ( $T_{\text{litho}} = 24$  km at 3.95 Gya) and those of Solomon and Head<sup>2</sup> ( $T_{\text{litho}} \geq 75$  km at  $\sim 3.0$  Gya). On the other hand, lunar thermal evolution model showed that the growth rate was  $\sim 75$  km/Ga during 3.95 to 3.0 Gya based on the result of Spohn *et al.*<sup>5</sup> (e.g., the curve showing 1073 K in their Fig. 2b), which is consistent with the result for the Smythii basin.



Finally, we discuss the volume and eruption rate of lava in the Smythii basin. The total thickness of the lava in the Smythii basin was 1.28 km<sup>16</sup> and the surface area of Mare Smythii was  $1.1 \times 10^5$  km<sup>2</sup>. Thus, the total volume of lava in Mare Smythii was  $\sim 1.4 \times 10^5$  km<sup>3</sup>, which is much higher than the volume of Unit 2 ( $6.6 \times 10^3$  km<sup>3</sup>) (Table S2); the Smythii basin is almost covered by the lava of Unit 1 ( $\sim 1.3 \times 10^5$  km<sup>3</sup>). The estimated eruption rate of the lava in Unit 1 was  $\sim 8.4 \times 10^{-4}$  km<sup>3</sup>/yr during 4.11 to 3.95 Gya, which is close to the average rate corresponding to the lunar near side maria ( $\sim 10^{-3}$  to  $\sim 10^{-5}$  km<sup>3</sup>/yr)<sup>24</sup>. This indicates that the volcanic activity in the Smythii basin was extremely intensive before 3.95 Gya. Thereafter, at least  $6.6 \times 10^3$  km<sup>3</sup> of lava erupted in Unit 2 by 3.07 Gya, the eruption rate being  $\sim 7.5 \times 10^{-6}$  km<sup>3</sup>/yr during 3.95 to 3.07 Gya, which is lower than the average rate for the lunar near side maria.

The eruption rate rapidly decreased after  $\sim 3.4$  Gya in the lunar nearside maria<sup>24</sup>, but after 3.95 Gya in the Smythii basin; the timing of decline in volcanic activity differs between the lunar nearside maria and the Smythii basin. The low eruption rate was caused by the increase in lithospheric thickness owing to lunar thermal cooling<sup>2</sup> or by the depletion of the lava source in the lunar mantle<sup>5</sup>. Therefore, the state of lunar thermal evolution probably differs among the lunar nearside, farside, and boundary between the two hemispheres (such as the location of the Smythii basin). If lunar thermal cooling was dominant, the growth of the lithosphere after 3.95 Gya ( $> \sim 60$  km/Ga) may have prevented the eruption of lava. A comprehensive understanding of volcanic history in various areas would shed light on the complexities of lunar thermal evolution.

## Methods

**Average depths of subsurface boundaries 1 to 4.** We used the LRS data to investigate the subsurface structures in the Smythii basin. The LRS is an observation instrument that performs global subsurface radar sounding<sup>25</sup> and transmits electromagnetic waves of 4–6 MHz at an interval of 75 m along the SELENE orbital track from an altitude of  $\sim 100$  km from the lunar surface. It measures the time delay difference between the surface and subsurface echoes ( $\Delta t$ )<sup>25</sup>. The LRS data cover the area spanning 8°S–5°N to 81°E–92°E (Fig. 1b), which includes 90 tracks. To eliminate clutter noise caused by lunar surface topography, we used synthetic aperture radar (SAR)-processed LRS data<sup>26</sup> [<http://darts.isas.jaxa.jp/planet/pdap/seleone/index.html.en>]. The elimination capability of noise was shown by Kobayashi *et al.*<sup>26</sup> (e.g., see their Figs 8 and 9). The synthetic aperture is 5 km, and the spatial resolution is  $\sim 0.8$  km along the orbital track direction and  $\sim 4$  km along the longitude direction. Based on the analysis of Ono *et al.*<sup>18</sup>, we identified four subsurface boundaries from the continuity of the subsurface echo along the latitude, and confirmed the existence of subsurface echoes between adjacent orbits.

The depth of the subsurface boundary at a local location ( $d_{\varepsilon_{\text{bulk}}}$ ) is given by

$$d_{\varepsilon_{\text{bulk}}} = \frac{c}{\sqrt{\varepsilon_{\text{bulk}}}} \cdot \frac{\Delta t}{2} = \frac{d_{\text{radar}}}{\sqrt{\varepsilon_{\text{bulk}}}}, \quad (1)$$

where  $c$  is the speed of electromagnetic wave in a vacuum ( $3 \times 10^8$  m/s),  $\varepsilon_{\text{bulk}}$  is the bulk permittivity of the subsurface layer, and  $d_{\text{radar}}$  is the apparent radar depth, which is calculated by assuming that  $\varepsilon_{\text{bulk}}$  is the same as that in a vacuum ( $\varepsilon_{\text{bulk}} = 1$ ). The bulk permittivity of lunar basalt is 4–11 based on the Apollo basalt samples<sup>27</sup>, mode value of which is 6 to 7 in permittivity histogram. In this study, we supposed that  $\varepsilon_{\text{bulk}} = 6$ , so the depth at local location ( $d_6$ ) is given as

$$d_6 = \frac{d_{\text{radar}}}{\sqrt{6}}. \quad (2)$$

If the standard deviation of permittivity is  $\pm 5$ , the subsurface boundary depth has the standard deviation of  $\sim 17\%$  with reference to  $d_{\text{radar}}$ .

We measured the depths ( $d_6$ ) of both ends of the continuous subsurface boundary along the latitude on the radargram. For example, the measured locations are shown on the surface echo (see the 10 white points on the surface echo shown in Fig. 2b). Subsequently, we estimated the average depth for each subsurface boundary ( $d_{\text{ave}}$ ) as

$$d_{\text{ave}} = \frac{\sum d_6}{N}, \quad (3)$$

where  $N$  is the total number of measured locations for a subsurface boundary, and  $\sum d_6$  is the summation of all average subsurface boundary depths. However, there are caveats in the calculation of Eq. 4. For example, we identified the outcrop of the subsurface boundary, edge depth of which is 0 m. We excluded the zero depth when using Eq. 3. The error of subsurface boundary depth was simply obtained from the standard deviation of the data set used in Eq. 3.

**Crater chronology.** To determine the surface ages of the Smythii basin, Unit 1, and Unit 2 based on the crater chronology, we first measured the crater size–frequency distribution (CSFD) for Unit 1. The CSFD was obtained using the SELENE/TC Ortho map data<sup>28</sup> (Fig. 4) [<http://darts.isas.jaxa.jp/planet/pdap/seleone/index.html.en>]. These data were resampled to the spatial resolution of  $\sim 74$  m/pixel. Subsequently, we fitted the measured CSFD to the crater production function (Eq. 4)<sup>4</sup>:

$$\log_{10} N(D) = a_0 + \sum_{k=1}^{11} a_k (\log_{10} D)^k, \quad (4)$$

where  $D$  is the crater diameter [km],  $N(D)$  is the cumulative number of craters per km<sup>2</sup> larger than  $D$ , and  $a_0$  and  $a_n$  are the coefficients based on the study by Neukum<sup>29</sup>. Thus,  $N(1)$ , that is, the cumulative number of craters on the grey curve of 10<sup>0</sup> km diameter (e.g. Fig. 4e), is obtained. Finally, we estimated the surface age of Unit 1 ( $t$  [Ga]) by substituting  $N(1)$  in the crater chronology function (Eq. 5)<sup>4</sup>:

$$N(1) = A \{ \exp(Bt) - 1 \} + Ct, \quad (5)$$

where  $A$ ,  $B$ , and  $C$  are the coefficients based on the study by Neukum<sup>29</sup>. To make these calculations smooth, we used Craterstats 2.0 software<sup>30</sup>. The error of surface age was based on the definition of previous study<sup>3</sup>.

**Radar reflection/transmission model.** We analytically calculated the echo intensity using a simple radar reflection/transmission model<sup>25</sup>. For example, we considered three layers (i.e., vacuum, Unit 1, and Unit 2) (Fig. S4). The intensity ratio of the surface and subsurface echoes is given as

$$\frac{P_{\text{subsurface}}}{P_{\text{surface}}} \approx \frac{R_{2,1}(1 - R_{0,2})^2}{R_{0,2}} \exp(-\Delta t \cdot 2\pi f \cdot \tan \delta), \quad (6)$$

where  $R_{0,2}$ ,  $R_{2,1}$ , and  $\tan \delta$  are as follows:

$$R_{0,2} = \left( \frac{\sqrt{\varepsilon_{\text{bulk}_0}} - \sqrt{\varepsilon_{\text{bulk}_2}}}{\sqrt{\varepsilon_{\text{bulk}_0}} + \sqrt{\varepsilon_{\text{bulk}_2}}} \right)^2, \quad (7)$$

$$R_{2,1} = \left( \frac{\sqrt{\varepsilon_{\text{bulk}_2}} - \sqrt{\varepsilon_{\text{bulk}_1}}}{\sqrt{\varepsilon_{\text{bulk}_2}} + \sqrt{\varepsilon_{\text{bulk}_1}}} \right)^2, \quad (8)$$

and

$$\tan \delta = 10^{0.045 \times C - 2.754}. \quad (9)$$

$R_{0,2}$  and  $R_{2,1}$  are reflection coefficients on the boundaries between the vacuum and Unit 2 and between Unit 2 and Unit 1 respectively,  $\Delta t$  is the time delay between the surface and subsurface echoes,  $f$  is frequency (5 MHz),  $\tan \delta$  is the loss tangent of Unit 2, and  $C$  is the mineral composition (TiO<sub>2</sub> + FeO [wt.%]).  $\varepsilon_{\text{bulk}_0}$  is the permittivity of vacuum ( $\varepsilon_{\text{bulk}_0} = 1$ ).  $\varepsilon_{\text{bulk}_1}$  and  $\varepsilon_{\text{bulk}_2}$  are the bulk permittivities of Units 1 and 2, which are approximated on the basis of the effective medium theory<sup>31</sup>:

$$\varepsilon_{\text{bulk}} = \varepsilon_{\text{grain}} + 3\varepsilon_{\text{grain}} \frac{b}{b - 1}, \quad (10)$$

and

$$b = \phi \frac{1 - \varepsilon_{\text{grain}}}{1 + 2\varepsilon_{\text{grain}}}. \quad (11)$$

$\phi$  is the porosity of the subsurface layer, and  $\varepsilon_{\text{grain}}$  is pore-free permittivity (i.e. grain permittivity) of the subsurface layer<sup>32,33</sup>.

$$\varepsilon_{\text{grain}} = 1.919\rho_{\text{grain}}, \quad (12)$$

where  $\rho_{\text{grain}}$  is given as

$$\rho_{\text{grain}} = 0.0273 \cdot \text{FeO} + 0.0110 \cdot \text{TiO}_2 + 2.773. \quad (13)$$

When the mineral compositions are such that TiO<sub>2</sub> = 1.54 wt.% and FeO = 8.73 wt.% for Unit 1 and TiO<sub>2</sub> = 4.15 wt.% and FeO = 16.66 wt.% for Unit 2 (Fig. 5) and  $\phi = 7\%$  based on the Apollo sample<sup>23</sup>,  $\varepsilon_{\text{bulk}_1}$  is 6.27 and  $\varepsilon_{\text{bulk}_2}$  is 7.27. If  $\Delta t = 3.33 \times 10^{-6}$  s based on the depth of the deepest subsurface echo (~500 m), the level of the subsurface echo is about -35 dB with respect to level of the surface echo as per Eq. 6. Considering that the permittivity of Unit 1 is equal to that of the regolith ( $\varepsilon_{\text{bulk}_1} = 2$ ), we can estimate that the echo level is about -17 dB using Eq. 6.

**Loading model.** We analytically calculated the subsidence of Unit 1 based on a simple loading model<sup>1</sup>. For example, we supposed a lava load (i.e. Unit 1) on the lithosphere (Fig. S5). In this study, the load has a radius  $r$  of 97.5 km with reference to the radius of Unit 2, a thickness  $h$  of 1.28 km, and bulk density  $\rho_{\text{unit1}}$ , and the lithosphere has a thickness  $T_{\text{litho}}$  of 24 km. The subsidence ( $w$ ) is given by the basic partial differential equation<sup>34</sup>.

$$\nabla^4 w + \frac{w}{\ell^4} = \frac{q}{A}, \quad (14)$$

where  $q$  is the load and  $\ell$  is the relative stiffness of the lithosphere.



$$q = \rho_{\text{unit1}} \cdot g \cdot h, \quad (15)$$

$$\ell^4 = \frac{A}{B}, \quad (16)$$

$$A = \frac{E \cdot T_{\text{litho}}^3}{12(1 - \nu^2)}, \quad (17)$$

and

$$B = \frac{E \cdot T_{\text{litho}}}{R^2} + \rho_m \cdot g. \quad (18)$$

$E$  is Young's modulus (=100 GPa),  $\nu$  is Poisson's ratio (=0.25),  $R$  is the lunar radius (=1737.4 km),  $\rho_{\text{unit1}}$  is given as  $\rho_{\text{grain}}(1 - \phi)$  based on Eq. 13 and mineral composition of Unit 1,  $\rho_m$  is the bulk density of the lunar mantle (=3400 kg m<sup>-3</sup>), and  $g$  is lunar gravity (=1.64 m s<sup>-2</sup>). If  $\phi = 7\%$ , TiO<sub>2</sub> = 1.54 wt.%, and FeO = 8.73 wt.% in Unit 1,  $\rho_{\text{unit1}} = \sim 2800$  kg m<sup>-3</sup>. The solution of Eq. 14 is approximately given as the function of the distance from the load's centre ( $x$ , dimensionless parameter):

$$w_{\text{in}}(x) = \frac{q \cdot a}{B}(\text{Ker}'a \cdot \text{Ber}x - \text{Kei}'a \cdot \text{Bei}x + 1/a)(x \leq a), \quad (19)$$

and

$$w_{\text{out}}(x) = \frac{q \cdot a}{B}(\text{Ber}'a \cdot \text{Ker}x - \text{Bei}'a \cdot \text{Kei}x)(x \geq a), \quad (20)$$

where  $w_{\text{in}}$  and  $w_{\text{out}}$  are subsidence inside and outside the load; Ker, Kei, Ber, and Bei are the Bessel–Kelvin functions of order zero; and the prime denotes the first derivative<sup>1</sup>.  $a$  is the load radius normalized by  $\ell$ .

$$a = \frac{r}{\ell}. \quad (21)$$

When  $x$  is 0, the maximum depth of subsidence is given by Eq. 19:

$$w_{\text{in}}(0) = \frac{q \cdot a}{B}(\text{Ker}'a + 1/a), \quad (22)$$

where  $\text{Ber}(0) = 1$ , and  $\text{Bei}(0) = 0$ . In this study,  $a = 1.47$  from Eq. 21 and  $\text{Ker}'(1.45) \approx -3.10$ . Thus,  $w_{\text{in}}(0) = 502$  m, which is consistent with the depth of deepest subsurface echo (~500 m) based on the LRS observation.

## References

- Solomon, S. C. & Head, J. W. Vertical movement in mare basins: relation to mare emplacement, basin tectonics, and lunar thermal history. *J. Geophys. Res.* **84**, 1667–1682 (1979).
- Solomon, S. C. & Head, J. W. Lunar mascon basins: Lava filling, tectonics, and evolution of the lithosphere. *Rev. Geophys.* **18**, 107–141, <https://doi.org/10.1029/RG018i001p00107> (1980).
- Hiesinger, H., Head, J. W., Wolf, U., Jaumann, R. & Neukum, G. Ages and stratigraphy of lunar mare basalts in Mare Frigoris and other nearside maria based on crater size-frequency distribution measurements. *J. Geophys. Res.-Planets.* **115**, E03003, <https://doi.org/10.1029/2009JE003380> (2010).
- Morota, T. *et al.* Timing and characteristics of the latest mare eruption on the Moon. *Earth Planet. Sci. Lett.* **302**, 255–266, <https://doi.org/10.1016/j.epsl.2010.12.028> (2011).
- Spohn, T., Konrad, W., Breuer, D. & Ziethe, R. The longevity of lunar volcanism: Implications of thermal evolution calculations with 2D and 3D mantle convection models. *Icarus.* **149**, 54–65, <https://doi.org/10.1006/icar.2000.6514> (2001).
- Ziethe, R., Seiferlin, K. & Hiesinger, H. Duration and extent of lunar volcanism: Comparison of 3D convection models to mare basalt ages. *Planet. Space Sci.* **57**, 784–796, <https://doi.org/10.1016/j.pss.2009.02.002> (2009).
- Ryder, G. Mass flux in the ancient Earth–Moon system and benign implications for the origin of life on Earth. *J. Geophys. Res.* **107**, 5002, <https://doi.org/10.1029/2001JE001583> (2002).
- Gomes, R., Levison, H. F., Tsiganis, K. & Morbidelli, A. Origin of the cataclysmic Late Heavy Bombardment period of the terrestrial planets. *Nature.* **435**, 466–469, <https://doi.org/10.1038/nature03676> (2005).
- Brennan, W. J. Evolution of Mare Smythii. *Abstracts of the Lunar and Planetary Science Conference.* **6**, 86 (1975).
- Stewart, H. E., Waskom, J. D. & DeHon, R. A. Photogeology and basin configuration of Mare Smythii. *Proc. Lunar Planet. Sci. Conf.* **3**, 2541–2551 (1975).
- Spudis, P. D. *The Geology of Multi-ring Basins: The Moon and Other Planets.* (Cambridge Univ. Press, Cambridge, 1993).
- Conca, J. & Hubbard, N. Evidence of early volcanism in Mare Smythii. *Proc. Lunar Planet. Sci. Conf.* **2**, 1727–1737 (1979).
- Wilhelms, D. E. & El-Baz, F. *Geologic Map of the East Side of the Moon.* (U.S. Geol. Surv., Denver, 1977).
- Gillis, J. J. & Spudis, P. D. Geology of the Smythii and Marginis region of the Moon: Using integrated remotely sensed data. *J. Geophys. Res.-Planets.* **105**, 4217–4233, <https://doi.org/10.1029/1999JE001111> (2000).
- Solomon, S. C. & Chaiken, J. Thermal expansion and thermal stress in the moon and terrestrial planets - Clues to early thermal history. *Proc. Lunar Planet. Sci. Conf.* **3**, 3229–3243 (1976).
- Williams, K. K. & Zuber, M. T. Measurement and analysis of lunar basin depths from Clementine altimetry. *Icarus.* **131**, 107–122, <https://doi.org/10.1006/icar.1997.5856> (1998).
- DeHon, R. A. & Waskom, J. D. Geologic structure of the eastern mare basins. *Proc. Lunar Planet. Sci. Conf.* **3**, 2729–2746 (1976).
- Ono *et al.* Lunar Radar Sounder observations of subsurface layers under the nearside maria of the Moon. *Science* **323**(5916), 909–912 (2009).

19. Kobayashi, T., Lee, S. R., Kumamoto, A. & Ono, T. GPR observation of the Moon from orbit: Kaguya Lunar Radar Sounder. *15th Int. Conf. Ground Penetrating Radar (GPR)*, 1037–1041, <https://doi.org/10.1109/ICGPR.2014.6970585> (2014).
20. Weider, S. Z., Crawford, I. A. & Joy, K. H. Individual lava flow thicknesses in Oceanus Procellarum and Mare Serenitatis determined from Clementine multispectral data. *Icarus* **209**(2), 323–336, <https://doi.org/10.1016/j.icarus.2010.05.010> (2010).
21. Ohtake, M. *et al.* Performance and scientific objectives of the SELENE (KAGUYA) Multiband Imager. *Earth Planets Space*. **60**, 257–264, <https://doi.org/10.1186/BF03352789> (2008).
22. Otake, H., Ohtake, M. & Hirata, N. Lunar iron and titanium abundance algorithms based on SELENE (Kaguya) Multiband Imager data. *43th Lunar Planet. Sci. Conf.* Abstract #1905 (2012).
23. Kiefer, W. S., Macke, R. J., Britt, D. T., Irving, A. J. & Consolmagno, G. J. The density and porosity of lunar rocks. *Geophys. Res. Lett.* **39**, L07201, <https://doi.org/10.1029/2012GL051319> (2012).
24. Oshigami *et al.* Mare volcanism: Reinterpretation based on Kaguya Lunar Radar Sounder data. *J. Geophys. Res. Planets*, **119**, 1037–1045, <https://doi.org/10.1002/2013JE004568> (2014).
25. Ono, T. & Oya, H. Lunar Radar Sounder (LRS) experiment on-board the SELENE spacecraft. *Earth Planets Space*. **52**, 629–637, <https://doi.org/10.1186/BF03351671> (2000).
26. Kobayashi, T. *et al.* Synthetic aperture radar processing of Kaguya lunar radar sounder data for lunar subsurface imaging. *IEEE T Geosci. Remote Sens* **50**, 2161–2174, <https://doi.org/10.1109/TGRS.2011.2171349> (2012).
27. Carrier, W. D. III, Olhoeft, G. R. & Mendell, W. Physical property of the lunar surface. In Heiken, G. H., Vaniman, D. T. & French, B. M. *Lunar Source Book: A User's Guide to the Moon*, 475–594, (Cambridge Univ. Press, New York, 1991).
28. Haruyama, J. *et al.* Global lunar-surface mapping experiment using the Lunar Imager/Spectrometer on SELENE. *Earth Planets Space*. **60**, 243–255, <https://doi.org/10.1186/BF03352788> (2008).
29. Neukum, G. Meteoritenbombardement und Datierung Planetarer Oberflächen. Habilitation Dissertation for Faculty Membership (Ludwig-Maximilians-Univ., Munich 1983).
30. Michael, G. G. Planetary surface dating from crater size–frequency distribution measurements: Multiple resurfacing episodes and differential isochron fitting. *Icarus* **226**(1), 885–890, <https://doi.org/10.1016/j.icarus.2013.07.004> (2013).
31. Ishiyama, K. *et al.* Effect of crack direction around laboratory-scale craters on mineral bulk permittivity. *Icarus* **319**, 512–524 (2019).
32. Ishiyama, K. *et al.* Estimation of the permittivity and porosity of the lunar uppermost basalt layer based on observations of impact craters by SELENE. *J. Geophys. Res. Planets* **118**, 1453–1467, <https://doi.org/10.1002/jgre.20102> (2013).
33. Huang, Q. & Wiczorek, M. A. Density and porosity of the lunar crust from gravity and topography. *Journal of Geophysical Research: Planets*. **117**, E05003, 1–9, <https://doi.org/10.1029/2012JE004062> (2012).
34. Brotchie, T. F. Flexure of a liquid-filled spherical shell in a radial gravity field. *Modern Geology* **3**, 15–23 (1971).
35. Araki, H. *et al.* Lunar global shape and polar topography derived from Kaguya-LALT laser altimetry. *Science*. **323**, 897–900, <https://doi.org/10.1126/science.1164146> (2009).

## Acknowledgements

We used observation data obtained by the SELENE spacecraft and would like to express our appreciation to all members of the SELENE project team for processing and analyzing the data. This study was supported by JLPEDA in ISAS/JAXA.

## Author Contributions

K.I. designed the study, wrote the manuscript, and produced the figures. A.K. contributed to improving the discussion with useful comments.

## Additional Information

**Supplementary information** accompanies this paper at <https://doi.org/10.1038/s41598-019-50296-9>.

**Competing Interests:** The authors declare no competing interests.

**Publisher's note** Springer Nature remains neutral with regard to jurisdictional claims in published maps and institutional affiliations.



**Open Access** This article is licensed under a Creative Commons Attribution 4.0 International License, which permits use, sharing, adaptation, distribution and reproduction in any medium or format, as long as you give appropriate credit to the original author(s) and the source, provide a link to the Creative Commons license, and indicate if changes were made. The images or other third party material in this article are included in the article's Creative Commons license, unless indicated otherwise in a credit line to the material. If material is not included in the article's Creative Commons license and your intended use is not permitted by statutory regulation or exceeds the permitted use, you will need to obtain permission directly from the copyright holder. To view a copy of this license, visit <http://creativecommons.org/licenses/by/4.0/>.

© The Author(s) 2019